PCCP

PAPER

A + B → C reaction fronts in Hele-Shaw cells under modulated gravitational acceleration

Kerstin Eckert,†*[a] Laurence Rongy†[b] and Anne De Wit[b]

The dynamics of A + B → C reaction fronts is studied under modulated gravitational acceleration by means of a combination of parabolic flight experiments and numerical simulations. During modulated gravity the front position undergoes periodic modulation with an accelerated front propagation under hyper-gravity together with a slowing down under low gravity. The underlying reason for this is an amplification and a decay, respectively, of the buoyancy-driven double vortex associated with the front propagation under standard gravitational acceleration, as explained by reaction–diffusion–convection simulations of convection around an A + B → C front. Deeper insights into the correlation between grey-value changes in the experimental shadowgraph images and characteristic changes in the concentration profiles are obtained by a numerical simulation of the imaging process.

1 Introduction

Gravitational acceleration is able to remarkably influence the propagation of reaction fronts in a variety of chemical systems. For example, it has long been known that autocatalytic fronts propagate with different speed in capillary tubes depending on the angle of inclination of the tube with regard to the vertical.[1] In spatially extended reactors, convective deformations of autocatalytic fronts into fingers have also been well characterised both experimentally and theoretically (see ref. 2–5 and references therein). Convection has been shown to affect reaction–diffusion travelling waves and spirals too, for instance in the emblematic Belousov–Zhabotinskii (BZ) reaction.[6] In liquid layers, convective motions perturb these waves leading to convective rolls and irregular patterns.[7]

For simple, irreversible chemical schemes such as A + B → C reactions, it has recently been shown that the reaction–diffusion properties of the related fronts[8,9] are not recovered if these fronts develop in the absence of gels allowing them to avoid convective motions. In vertical reactors for which the contact line between miscible solutions of A and B is perpendicular to the gravity field, convective patterns developing rapidly due to differences in densities between the reactant and product solutions have been observed for acid–base fronts for instance.[10–13] Similar convective patterns have also been obtained in immiscible two-layer systems where the dynamics can sometimes become even more complicated due to the presence of surface-tension driven Marangoni flows.[14,15]

In thin horizontal liquid layers where gravity points across the thin layer, one could think that the influence of buoyancy-driven motions is minimal. Nevertheless, Shi and Eckert[16] have evidenced that, although the well known square root of time displacement of reaction–diffusion A + B → C fronts[8] is recovered, the corresponding effective diffusion coefficient is more than ten times larger than the molecular diffusion coefficient, even for small layer thickness of the order of 1 mm. Furthermore, a faster progression with speed increasing when the thickness of the liquid layer is increased is observed, pointing to the tantamount role played by convection on such fronts in liquid layers. Rongy *et al.*[17,18] have numerically studied the nonlinear dynamics characterised by one or two flow vortices developing in horizontal cells around A + B → C fronts in the presence of density differences. They have furthermore classified all possible density profiles and related flow properties in a parameter space spanned by the Rayleigh numbers of the problem. However, no direct comparison between experiments and these theoretical predictions has been done yet. Here, we provide experimental support to this reaction–diffusion–convection (RDC) theory and show that it can be used to understand situations on earth but also more complicated scenarios with modulated gravity.

Experimental studies under microgravity conditions help understand the influence of buoyancy on the dynamics of RDC systems. For autocatalytic fronts, experiments in the BZ-system under microgravity (μg) conditions in drop towers[19,20] clearly show that the distinct differences in dynamics on earth between up- and downward or horizontal propagation vanish under μg where in the absence of convection all fronts, irrespective of

[a] *Institute of Fluid Mechanics, Technische Universität Dresden, D-01062 Dresden, Germany. E-mail: Kerstin.Eckert@tu-dresden.de; Fax: +49 351 463 33384; Tel: +49 351 463 34636*
[b] *Nonlinear Physical Chemistry Unit, Service de Chimie Physique et Biologie Théorique, Faculté des Sciences, Université Libre de Bruxelles (ULB), CP 231, 1050 Belgium*
† These authors contributed equally to this work.

their propagation direction, display the same speed. For A + B → C reactions in immiscible two-layer systems, microgravity conditions are crucial to isolate Marangoni effects from buoyancy ones. Experiments in sounding rockets have clearly shown that under microgravity, the dynamics is totally different than on earth. In particular, dominant Marangoni effects allow there strong deformations of the interface[21] and suppression of the buoyancy-driven fingering obtained both above and below the interface in vertical systems on earth.[14,15,22]

In this context, we show here that microgravity experiments also provide important insight into the dynamics of A + B → C fronts in horizontal layers. Comparison between dynamics of A + B → C fronts measured experimentally during parabolic flights with those obtained on earth[16] confirms that, even in thin liquid layers, convective motions drastically influence the properties of such fronts. In periodically modulated gravitational acceleration, we observe indeed a periodic change from an accelerated front propagation under hyper-gravity towards a slowed down motion under low gravity. These results are backed up by numerical integration of a RDC model focusing on the A + B → C front obtained when two miscible solutions containing A and B, respectively, are brought into contact. These simulations confirm the experimental behaviour and make visible the underlying changes in the buoyancy-driven flow field consisting of a double vortex whose up-flow is at the reaction front position. Furthermore, by simulating the experimental shadowgraph imaging, a correlation between changes of the grey values in the experimental images with those of the concentration fields can be established.

2 Chemical system and experimental setup

The experimental container is a Hele-Shaw (HS) cell, schematically depicted in Fig. 1a. The HS cell is made of two 10.0 mm-thick borosilicate glass plates, with a 1 mm-thick PTFE sheet in between, which were integrated into an aluminium frame. The design and operation of the HS cell is described in detail in ref. 23. It allows a rapid filling of the reactive fluid–fluid system with a minimum of shear flow, together with the formation of a plane interface between the fluids.

The organic phase is a solution of propionic acid (CH_3–CH_2–$COOH$, concentration a_0) in cyclohexane, while the aqueous phase is formed by a solution of tetramethyl-ammoniumhydroxide (TMAH, $[CH_3]_4N^+OH^-$), the concentration of which is b_0. During the three flight days, three different concentration combinations with a ratio of $\beta = b_0/a_0 = 0.5$ were employed: (1) first day, $a_0 = 0.5$ M, $b_0 = 0.25$ M, (2) second day, $a_0 = 0.65$ M, $b_0 = 0.325$ M, and (3) third day, $a_0 = 1.5$ M, $b_0 = 0.75$ M where M abbreviates mol l^{-1}.

As soon as both phases come into contact, the weakly surface-active propionic acid (A) undergoes a mass transfer into the aqueous layer and is subsequently neutralised by the base TMAH (B), producing a salt, tetramethylammonium propionate (S), according to A + B → S. The resulting hydrodynamic instabilities in ground experiments have been well characterised in ref. 15 and 16. In a vertical HS cell, an entirely buoyancy-driven cellular pattern is formed in the aqueous phase between the interface and the propagating reaction front.[15] By contrast, in a horizontal HS cell this sort
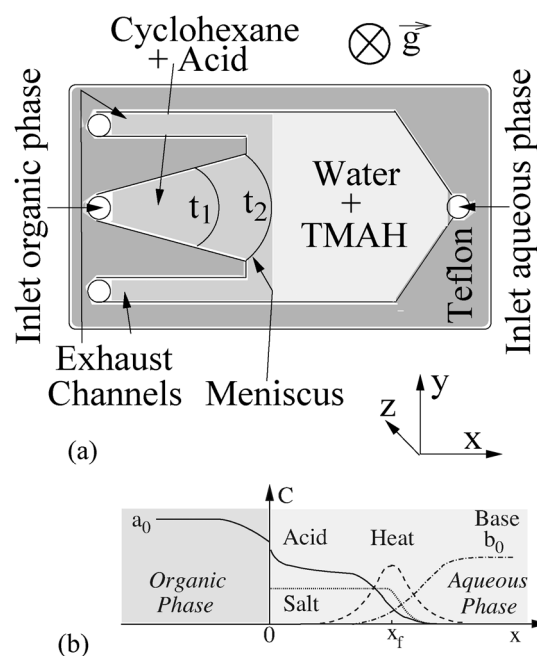

Fig. 1 (a) Sketch of the Hele-Shaw (HS) cell and of the chemical system filled into the HS cell. (b) Schematic diagram of the reaction–diffusion profiles of the reactive liquid–liquid system.

of pattern vanishes in favour of an unsteady Marangoni convection which leads to an acceleration of the reaction front propagation[16] compared to ref. 15. The main processes in the horizontal HS cell are summarised in Fig. 1b. In the aqueous phase located here on the right-hand side of the liquid–liquid interface at $x = 0$, the moving reaction front is visible. It is characterised by a sharp drop in the acid and base concentrations in favour of the salt production. For $a_0 > a_0^c$ with $a_0^c = 0.8$ mol l^{-1}, an unsteady cell-like convection appears along the interface, driven to a large extent by Marangoni effects.[16,24] Such large concentrations have been used only during the third flight day where convection is present for a short time span of about $t \approx 10$ min only. For the first and second flight days, $a_0 < a_0^c$ and Marangoni convection is therefore not present. Thus, as in all flights Marangoni effects are either absent or very limited, the main phenomenon to be studied is the propagation of the reaction front in the aqueous phase.

The reaction front in the HS cell is made visible by means of the shadowgraph technique.[25] For this purpose the HS cell is placed in between the two main lenses of a shadowgraph system (Thalheim Special Optics, Germany). Here the light of a green high-power LED is collimated by the first lens. Upon traveling through the HS cell, a light deflection occurs due to the optical inhomogeneities driven by the concentration fields. The resulting grey-value distribution is imaged onto the chip of a CCD camera (DALSA 21-2M30, 1600 × 1200 px) and grabbed with a rate of 10 frames per second, using a 2 × 2 binning mode. The shadowgraph technique is sensitive with respect to the Laplacian of the refractive index n. The shadowgraph produces a relative change in the light intensity, $(I - I_0)/I_0$ according to ref. 25

$$\frac{I - I_0}{I_0} = L_z \int_{z=0}^{z=L_z} \left(\frac{\partial^2}{\partial x^2} + \frac{\partial^2}{\partial y^2} \right) \ln(n) \, \mathrm{d}z, \qquad (1)$$
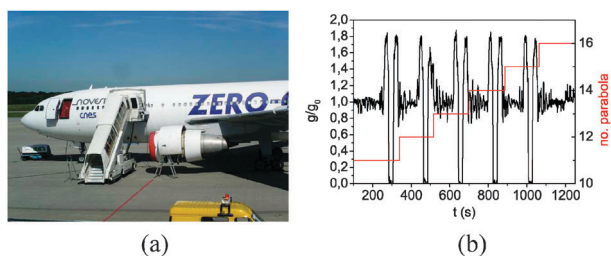
(a)   (b)

Fig. 2 (a) Zero-g airbus and (b) characteristic flight protocol of the gravitational acceleration *versus* time during different parabolas (red) which is shown exemplarily for a subset of 5 parabolas ($|\vec{g}_0| = 9.81$ m s^{-2}).

where L_z is the gap width of the cell and z is the direction perpendicular to the plates of the cell. The reaction front position X_f is extracted from the shadowgraph images by means of an edge-detection algorithm operating with sub-pixel accuracy by using an image processing software (HALCON, MVTec GmbH, Munich). For $a_0 < a_0^c$, the reaction front propagates parallel to the interface with exception of narrow regions close to the wall. In this case, X_f is obtained by averaging $X_f(y)$ over the entire straight part of the front. For $a_0 > a_0^c$, the locally varying intensity of the initial Marangoni convection leads to a curvature of the front with respect to the interface. In this case we average the $X_f(y)$-values of the fastest moving part of the front in a window of length $y = 10$ mm.

The shadowgraph optics together with the HS cell are assembled inside an aluminium container (1.6 m × 0.6 m × 0.6 m) which is installed on the rail system of the Zero-g airbus shown in Fig. 2a. To comply with the Zero-g-Airbus safety requirements, the aluminium container was completely sealed with no possibility of any direct interaction with the HS cell during the entire flight. For this reason, a pair of motor-driven syringes (HAMILTON), including PTFE tubes and 3-way valves, was additionally placed in the aluminium container in order to fill the HS cell semi-automatically *via* software, analogously to ref. 21. The filling was started once the airbus has passed the first of the 30 parabolas. Fig. 2b shows a section of the flight protocol, according to which, one parabola comprises two 20-second-phases of hyper-gravity ($g = 1.8g_0$ with $g_0 = 9.81$ m s^{-2}) which sandwich a phase of low-gravity ($10^{-2}g_0$). The results presented here were obtained during the 46th ESA parabolic flight campaign in Bordeaux.

3 Theoretical model and parameters

To reduce complexity, the simulations focus entirely on the aqueous phase, instead of treating the complete liquid–liquid system with the mass transfer through the interface. Thus we consider a two-dimensional (2D) thin aqueous solution layer of length L_x and height L_z oriented horizontally in the gravity field $\vec{g}$ in which an acid–base reaction, A + B → S, takes place, where A corresponds here to propionic acid, B to TMAH, and S (instead of C) to the *salt* tetramethylammonium propionate (see Fig. 3). This approach is justified first because, after some minutes only, the reaction front is already sufficiently far from the interface. Second, the Marangoni convection is either not present because $a_0 < a_0^c$ (first and second flight days) or has already decayed (third flight day). The isothermal
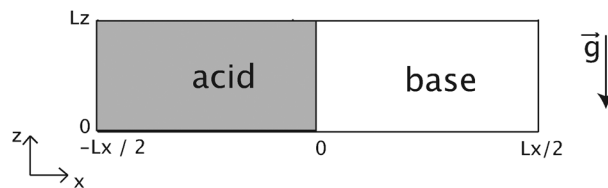

Fig. 3 Sketch of the system used in the numerical simulations.

governing equations for the acid, base, and salt concentrations, a, b, and s, respectively, are reaction–diffusion–convection equations. As shown in similar acid–base systems studied in HS geometries,[12] the heat contribution to density changes is here at least an order of magnitude smaller and can be safely neglected. The evolution of the 2D velocity field, $\vec{v} = (v_x, v_z)$, is described by the incompressible Stokes equations. We assume a linear dependence between the solution density, ρ, and the concentrations. We use the following characteristic scales of the reaction–diffusion system: $\tau_c = 1/ka_0$ for time, $L_c = \sqrt{D_a\tau_c}$ for length, $U_c = \sqrt{D_a/\tau_c}$ for velocity, $p_c = \mu/\tau_c$ for pressure and a_0 for concentration, where k is the kinetic constant of the acid–base reaction, a_0 is the initial concentration of the acid, D_a is its molecular diffusion coefficient, and μ is the dynamic viscosity. The resulting dimensionless equations read[17,18]

$$\frac{\partial a}{\partial t} + (\vec{v}\cdot\nabla)a = \nabla^2 a - ab \tag{2}$$

$$\frac{\partial b}{\partial t} + (\vec{v}\cdot\nabla)b = \delta_b\nabla^2 b - ab \tag{3}$$

$$\frac{\partial s}{\partial t} + (\vec{v}\cdot\nabla)s = \delta_s\nabla^2 s + ab \tag{4}$$

$$\nabla p = \nabla^2 \vec{v} - (R_a a + R_b b + R_s s)\vec{e}_z \tag{5}$$

$$\mathrm{div}\,\vec{v} = 0 \tag{6}$$

where p denotes the dynamic pressure above the background hydrostatic value, $\delta_{b,s} = D_{b,s}/D_a$ are the ratio between the molecular diffusion coefficients of the base and the salt, respectively, and that of the acid. The dimensionless Rayleigh numbers, $R_{a,b,s}$, are defined as

$$R_i = \frac{\partial \rho}{\partial c_i}\frac{a_0 L_c^3 g}{D_a \mu}, \tag{7}$$

where c_i is the dimensional concentration of the relevant species. The solutal Rayleigh numbers $R_{a,b,s}$ are positive as the corresponding solutes increase the density. We note that the use of Stokes equations is justified by the fact that, in our choice of non-dimensionalization, the inertial terms in the Navier–Stokes equations for the flow field would be divided by a Schmidt number, Sc $= \nu/D \approx 10^3$ for our system (see Table 2). In a previous study for similar systems,[26] it has been shown that a change in the value of Sc, if taken in this experimental range, does not affect the obtained results, meaning that inertial effects are negligible in these slow flow regimes compared to the viscous effects.

At every boundary of the domain, we require zero-flux boundary conditions for the concentrations and no-slip boundary conditions for the fluid velocity field. The initial conditions are:

$$x < 0, \forall z: s = 0, a = 1, b = 0$$

$$x > 0, \forall z: s = 0, a = 0, b = \beta$$

with $\beta = b_0/a_0$ the ratio between the initial concentrations of base and acid. The numerical method implemented to solve this system of equations is described in our previous articles.[17,18]

Using the values of parameters in Tables 1 and 2 and an average value of the experimental initial concentrations of acid, $\langle a_0 \rangle = 0.8$ M, we find $R_a = 2.7/k^{3/2}$, $R_b = 2.1/k^{3/2}$, and $R_s = 1.15/k^{3/2}$ (cf.: eqn (7)). Due to uncertainties in the chemical reaction constant k, we aim at a qualitative comparison with the experimental results and therefore choose the following Rayleigh numbers $R_a = 27$, $R_b = 21$, and $R_s = 11.5$. The ratio of the Rayleigh numbers is hence the same as the ratio of the experimental $\partial\rho/\partial c_i$. The initial concentration ratio is taken as in the experiment, i.e., $\beta = 0.5$. The choice of the diffusivity ratios $\delta_b = 0.5 = \delta_s$ is motivated by the fact that the base is a large molecule supposed to diffuse more slowly than the acid. The salt and the base, having close molecular formulas, should have similar diffusion coefficients.

To simulate the gravity modulations of the parabolic flight we let the normalised magnitude of the gravitational acceleration, g/g_0, with $g_0 = 9.81$ m s^{-2}, vary with time as shown in Fig. 4. Note that the non-dimensional time is expressed in units of the chemical time scale τ_c. Because the latter is not precisely known, we assume a duration of the hyper-g and low-g phases equal to $\Delta t = 500$. During the period of low-g, i.e., between $t = 1500$ and $t = 2000$, g is set equal to $0.1g_0$ rather than 0 in order to simulate inertial effects that cannot be present otherwise in a Stokes description of the velocity field.

4 Results and discussion

4.1 Experiments

Fig. 5 shows a key experimental result obtained during one of the three flight days by displaying the front position X_f versus time during 8 parabolas. In parallel, shadowgraph images belonging to characteristic stages of this curve are shown in Fig. 6. Fig. 5 indicates a representation of the reaction front under parabolic flight conditions by means of two characteristic lines, the leading edge and the trailing edge, the meaning of which is shown in the shadowgraph of Fig. 6c. The leading edge (LE) refers to the dark part of the reaction front directed towards the fresh aqueous phase while the trailing edge (TE)

Table 1 Solutal volume expansion coefficient $\partial\rho/\partial c_i$ from ref. 15

Species	$\partial\rho/\partial c_i$/kg l (mol m^3)$^{-1}$
Propionic acid	6.9
Base (TMAH)	5.6
Salt (TMA–propionate)	$\sim$3

Table 2 Material properties

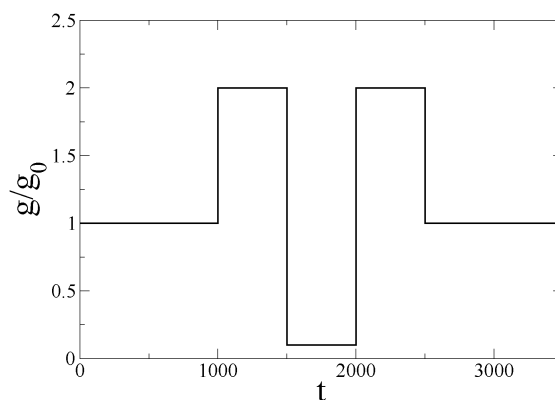| Property	Value
Density of water, ρ	0.998×10^3 kg m^{-3}
Kinematic viscosity of water, ν	0.96×10^{-6} m^2 s^{-1}
Mass diffusivity of propionic acid, D_a	1.11×10^{-9} m^2 s^{-1}

Fig. 4 The type of modulation of the normalised magnitude of the gravitational acceleration, g/g_0, as applied in the numerical simulations.
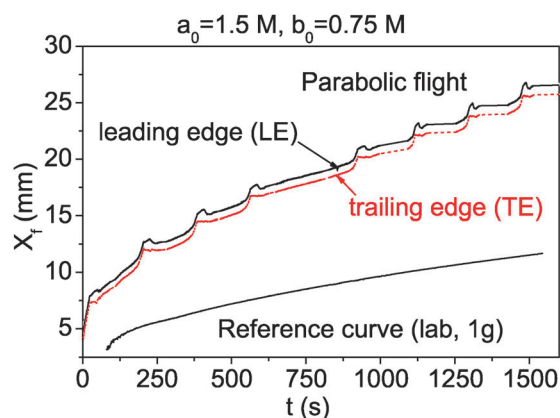

Fig. 5 Front position X_f versus time. Comparison between the parabolic flight and the laboratory experiment in the presence of Marangoni convection ($a_0 = 1.5$ M, $b_0 = 0.75$ M). The meaning of LE and TE is explained in the text.

marks the light edge behind characterized by a high grey value in the shadowgraph. The relationship between these lines and characteristic changes in the second derivative in the refractive index is clarified by means of the numerical simulations in Sec. 4.2. Under laboratory conditions a differentiation into LE and TE is not necessary since the distance between both curves does not change notably. Hence, they were averaged to obtain one line in the X_f-representation as in Fig. 5.

Coming back to Fig. 5, three distinct differences can be noted when comparing with the reference curve of the corresponding laboratory experiment under standard gravitational acceleration of $g_0 = 9.81$ m s^{-2}. First, the X_f-values of the LE- and TE-position pass characteristic undulations under the parabolic flight conditions. Second, the front propagation proceeds nearly three times faster than under normal laboratory conditions. Third, the detachment of the reaction front from the liquid–liquid interface occurs earlier under parabolic flight conditions. This is related to the fact that the early Marangoni convection (cf. Fig. 6a) present at the chosen initial concentrations ($a_0 = 1.5$ M, $b_0 = 0.75$ M) is superposed to twice a hyper-g-phase being responsible for this acceleration.

Next we examine the above-mentioned undulations of X_f which the system experiences after the start of the chemical
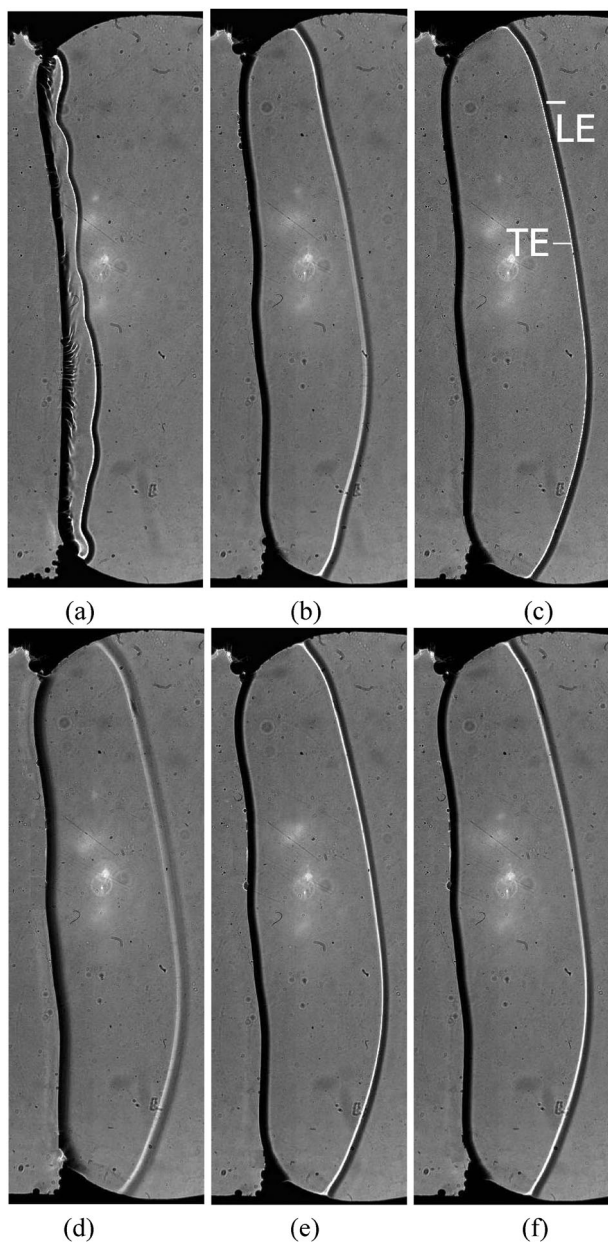
(a) (b) (c)

(d) (e) (f)

Fig. 6 Shadowgraph images of the reaction front during different stages of the experiment in Fig. 5: (a) Marangoni convection at $t = 12$ s, (b) front under normal-g at $t = 180$ s, (c) end of the first hyper-g phase of the second parabola ($t = 204$ s), (d) end of the low-g phase ($t = 226$ s), (e) end of the second hyper-g-phase ($t = 247$ s) and (f) front shape under normal-g ($t = 265$ s) ($a_0 = 1.5$ M, $b_0 = 0.75$ M). The position of the leading (LE) and trailing (TE) edges is shown. The size of the images is 42 mm × 15 mm.

reaction. Fig. 7 provides a zoom into the second parabola of Fig. 5 and shows the positions of the leading (LE) and trailing (TE) edges, X_f^{LE} and X_f^{TE}, respectively, during one parabola. In parallel we correlate in this figure the behaviour of both lines with the level of gravitational acceleration obtained upon synchronising the internal time of the PC used to grab the shadowgraph images with the flight protocol from which Fig. 2 shows a section. With the onset of the first hyper-g-phase both X_f^{LE} and X_f^{TE} strongly increase, hence, the front
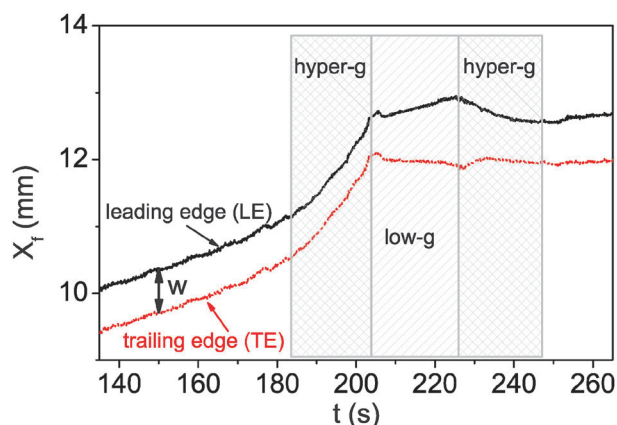

Fig. 7 Behaviour of X_f^{LE} and X_f^{TE} of leading and trailing edges *versus* time during different stages of the second parabola of Fig. 5 ($a_0 = 1.5$ M, $b_0 = 0.75$ M).

experiences an acceleration. However with the onset of the low-g phase both curves behave differently. While the LE-curve still advances, although with a much smaller slope, the TE-curve stagnates. This behaviour of TE is only marginally changed during the second hyper-g-phase. By contrast, the propagation of the LE front now proceeds in a reversed direction to move again towards the TE position. It is obvious that the different behaviour of both curves gives rise to a temporarily varying thickness $w = X_f^{LE} - X_f^{TE}$ of the shadowgraph representation of the reaction front which is shown for several parabolas in Fig. 8. While the shadowgraph displays a front thickness of about $w = (0.7 \pm 0.1)$ mm under $1g_0$, the thickness increases to $w = (1.1 \pm 0.1)$ mm under low-g. The shadowgraph images of these different g-phases in Fig. 6 underline this behaviour. We always notice a sharpening of the front in the hyper-g-phases accompanied by an increase of the contrast. During the low-g phase a fading out of the front over a larger area is observed (Fig. 6d). With every further parabola we notice that the contrast of the front progressively decreases under low-g. Thus, one could assume that the reaction front would no longer be visible in the shadowgraph for the hypothetic case of a very long low-g phase.

Fig. 9 shows the front position X_f *versus* time at reduced concentrations ($a_0 = 0.5$ M, $b_0 = 0.25$ M) but the same $\beta = b_0/a_0 = 0.5$. It reproduces all features already discussed in Fig. 5.
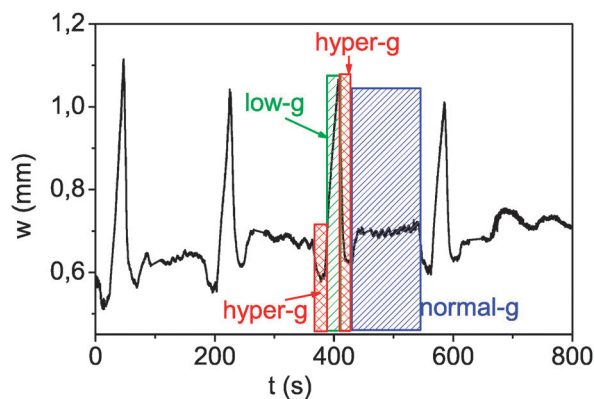

Fig. 8 The front width w evolution during four parabolas of Fig. 5 ($a_0 = 1.5$ M, $b_0 = 0.75$ M).
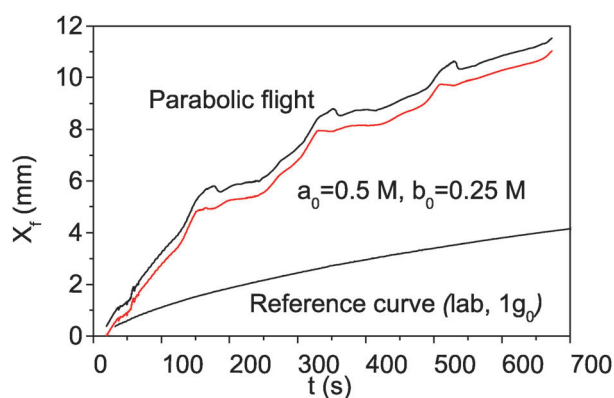
Fig. 9 The behaviour of the front position X_f at reduced concentration without Marangoni convection ($a_0 = 0.5$ M, $b_0 = 0.25$ M) in comparison between laboratory and parabolic flight experiments. For the latter again X_f^{LE} and X_f^{TE} (red curve) are shown.

Again, the front propagation is approximately a factor three faster than in the corresponding ground-reference experiment together with an earlier detachment of the front from the interface. The same type of characteristic undulations is present in the positions of the leading and trailing edges.

Within the resolution of the shadowgraph imaging and the subsequent image processing we could not detect significant structural changes between the X_f-undulations belonging to different initial concentrations as can be seen in Fig. 10. It shows the parabolic flight curves of Fig. 5 and 9 together while the latter curve is artificially shifted both in time, to achieve an overlap with respect to the onset of the first low-g phase shown, and in the vertical direction for better comparability.

4.2 Numerical simulations

In addition to the experimental diagnostics operating in transmission through the Hele-Shaw cell along the z-axis, the numerics also gives access to the spatial distribution of the reactants along the x- and z-axes inside the thin gap of the HS cell. Starting from the initial conditions depicted in Fig. 3, we let RDC processes operate under the modulated gravity conditions in Fig. 4. The corresponding concentration fields of acid and base are plotted in Fig. 11 during the normal-g (top), hyper-g (middle) and low-g (bottom) phases. In the first two phases, a bending of the iso-contours at the top plate towards
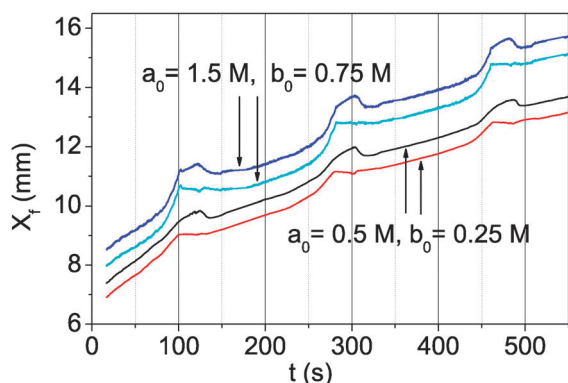
Fig. 10 Comparison of the X_f^{LE} and X_f^{TE} positions between different initial concentrations (1st and 3rd flight days).
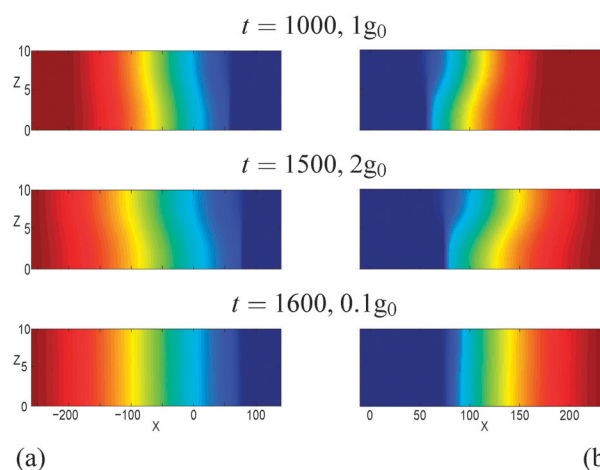
Fig. 11 Concentration fields of (a) the acid ranging from $a = a_0$ to the left (red) to $a = 0$ to the right (blue), and (b) the base ranging from $b = 0$ to the left (blue) and $b = \beta$ to the right (red). The snapshots are shown at the ends of both the normal-g (top line, $t = 1000$) and the hyper-g (middle, $t = 1500$) phases, and during the low g-phase (bottom, $t = 1600$).

the unperturbed concentration is visible in both the acid and the base sides. This is a direct consequence of advection of the species concentrations by the flow field which is shown in Fig. 12, superimposed on the salt concentration. This advection is almost suppressed and the bending hence cancelled in the low-g phase (see the 4th panel of Fig. 12). Convection occurs because the salt produced by the reaction is less dense than the reactants ($R_s = 11.5 < R_b = 21 < R_a = 27$) and rises between the acid and the base.[17,18] The flow field is hence characterised by two counter-rotating vortices. As the difference in densities is larger between the acid and the salt than between the base and the salt, the left vortex has a stronger intensity. There is thus a mean displacement to the right as evidenced by the fact that the location of salt production (Fig. 12) is in the $x > 0$ zone. Moreover, since the flows, coming from both sides, converge at the bottom but diverge at the top, the iso-contour lines are stretched there but compressed at the bottom which explains the type of bending visible in Fig. 11 and 12.

The forcing of both vortices results from buoyancy provided by the conversion of the respective reactants, A and B, into the lighter salt. Consequently, the place where the up-flow occurs is the place of maximum salt concentration (see Fig. 12), *i.e.*, at the position X_f where the depth-averaged production rate $\langle ab \rangle$ is maximum as will be shown later on. When inspecting the changes of both flows and concentrations within the g-profile of Fig. 4 in more detail, we note a most vigorous convection in the hyper-g phase, as expected because the Rayleigh numbers, eqn (7), scale with the level of g. As a result, the bending of the iso-concentration contours increases both with the level of g and the duration of the respective buoyancy-driven convection regime, *cf.* the changes between $t = 1100$ and $t = 1500$ or those between $t = 2100$ and $t = 2500$ (hyper-g). We also note that the intensity of the flow field decreases with time within each g-phase because the more bent the iso-concentration contours, the smaller the concentration gradients, and hence the smaller the density gradients, leading to weaker buoyancy-driven flows.
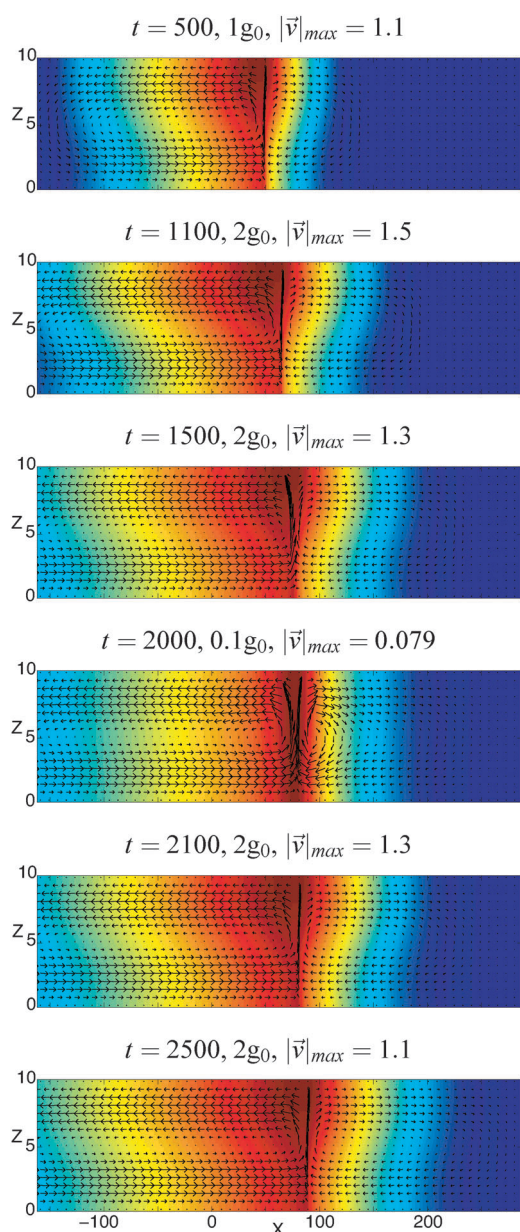
Fig. 12 Velocity field superimposed on the salt concentration field ranging from $s = s_{max}$ in the middle (red) to $s = 0$ on the sides (blue) at different times. The velocity vectors have been rescaled in each plot to optimise their size. Their maximum intensity, $|\vec{v}|_{max}$, is given for each plot, showing that the velocities are much smaller in the low-g phase.

During the low-g phase the convection is drastically diminished to a small level set by the remaining gravity level of $0.1g_0$.

Physically, the relationship between the concentration fields, in Fig. 11 and 12, and the refractive index n is as follows:

$$n = n_0 + \sum_{i=1}^{3} \frac{\partial n}{\partial c_i^*} c_i^*(x, z) \qquad (8)$$

with the reference refractive index of pure water $n_0 = 1.333$, $\frac{\partial n}{\partial a^*} = 0.0061 \ 1 \ mol^{-1}$, $\frac{\partial n}{\partial b^*} = 0.017 \ 1 \ mol^{-1}$, $\frac{\partial n}{\partial s^*} = 0.0201 \ 1 \ mol^{-1}$.[15] Note that the starred quantities, c_i^*,

a^*, b^* and s^*, refer to the dimensional concentrations. To simulate the shadowgraph imaging which captures the curvature of refractive index changes, we differentiate eqn (8) twice with respect to x and integrate over the layer thickness L_z to obtain the second derivative of the depth-averaged refractive index, $d^2\langle n \rangle/dx^2$. Since integration and differentiation can be exchanged we finally arrive at eqn (10).

$$\frac{d^2\langle n \rangle}{dx^2} = \frac{1}{L_z} \int_0^{L_z} \sum_{i}^{3} \frac{\partial n}{\partial c_i^*} \frac{\partial^2}{\partial x^2} c_i^* \ dz \qquad (9)$$

$$= \frac{a_0}{L_z} \sum_{i}^{3} \frac{\partial n}{\partial c_i^*} \frac{\partial^2}{\partial x^2} \int_0^{L_z} c_i \ dz$$

$$= a_0 \sum_{i}^{3} \frac{\partial n}{\partial c_i^*} \frac{d^2\langle c_i \rangle}{dx^2} \qquad (10)$$

This equation states that the second derivative of the depth-averaged refractive index, as monitored by the shadowgraph, is related to the sum of the second derivative of the depth-averaged species concentrations, weighted by $\partial n/\partial c_i^*$, the dependence of n on their concentration. In Fig. 13 we show the spatial evolution of $d^2\langle n \rangle/dx^2$ and $\langle c_i \rangle$. During hyper-g we see that $d^2\langle n \rangle/dx^2$ is zero everywhere (Fig. 13a), implying a constant grey-value distribution in the shadowgraph, with exception of a localised spot where it undergoes a sudden change including a sign reversal. This marks a crossover from a bright contour, the *trailing edge* (*cf.* Fig. 6), where $d^2\langle n \rangle/dx^2$ is maximum, towards a dark contour, the *leading edge* where $d^2\langle n \rangle/dx^2$ has a local minimum, see Fig. 6. A comparison with $\langle c_i \rangle$ in Fig. 13b and d shows that the x-position of the maximum of $d^2\langle n \rangle/dx^2$ correlates to the maximum salt concentration $\langle s \rangle_{max}$. This is caused by the fact that (i) a notable change in the curvature of $\langle c_i \rangle$ occurs only in the vicinity of $\langle s \rangle_{max}$ and (ii) the salt possesses the highest $\frac{\partial n}{\partial c_i^*}$. By contrast, the minimum belonging to the leading edge is the result of an antagonistic action of the salt and base concentration profiles. The local minimum and maximum observed in the acid region correspond to a change in curvature of the salt profile. In the low-g phase, $d^2\langle n \rangle/dx^2$ is much more extended spatially and reduced by a factor 50 (compare Fig 13a and c) because diffusion smearing all profiles is temporarily taking over convection.

The positions of the leading and trailing edges, as deduced from the positions of minimum and maximum $d^2\langle n \rangle/dx^2$, during one period of g-modulation are plotted in Fig. 14a. In parallel we show the position of the reaction front X_f, defined in the numerics as the point along the x axis where the depth-averaged production rate $\langle ab \rangle$ is maximum, compared with the front position under standard gravitational acceleration $g/g_0 = 1$. First note that the position of the reaction front X_f is in between the positions of the leading and trailing edges. Second, we observe again the characteristic modulations of the front position as already found in the experiments, *cf.* Fig. 7. While in the normal-g phase up to $t = 1000$, the curve simulating the parabolic flight environment is identical to the $g/g_0 = 1$ curve, the reaction front is accelerated compared to its counterpart in normal gravity as soon as the hyper-gravity
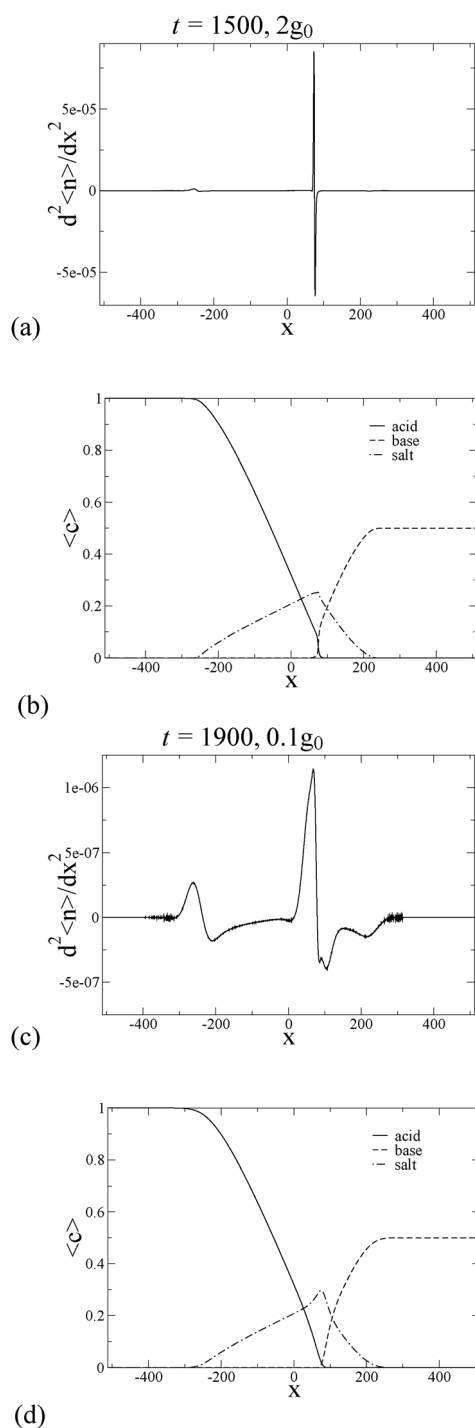
(a)

(b)

(c)

(d)

Fig. 13 Second derivative of the depth-averaged refractive index in units of a_0 together with the depth-averaged concentration profiles at two different times during the first hyper-gravity phase (a–b) and during the microgravity phase (c–d).

phase starts. By contrast, when entering the low-g phase, the reaction front velocity is drastically diminished. In very close agreement with the experiment in Fig. 7, this behavior is accompanied by opposite changes in the leading edge, which still undergoes propagation, and the trailing one which soon comes to a stagnation. The resulting behavior of the front width is plotted in Fig. 14b. In analogy to the experiment an
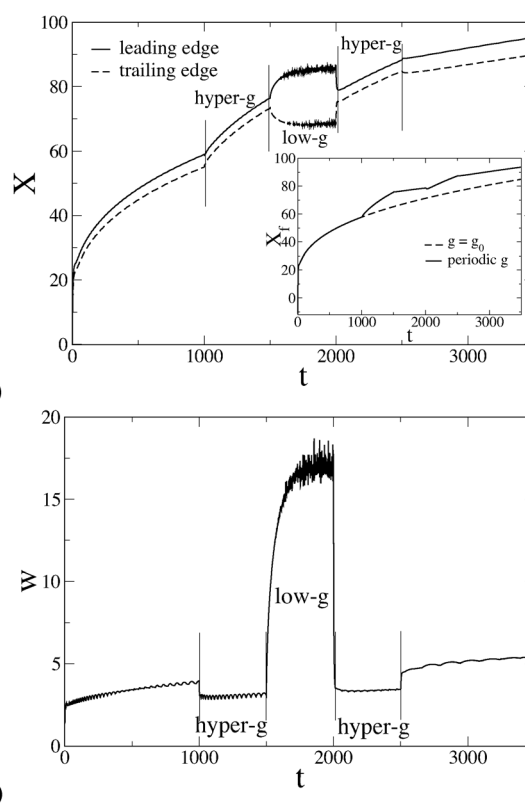

Fig. 14 (a) Position of the leading and trailing edges, extracted from Fig. 13. The inset shows the maximum value of the depth-averaged production rate X_f as a function of time under normal gravity and periodic gravity conditions. (b) Spatial difference between leading and trailing edges.

increase of the front width w is also detected in the simulations during the low-g phase, together with a reduction of w during the hyper-g phases.

4.3 Interpretation of velocity and shadowgraphy data

As demonstrated in the previous section, the numerical simulations of the RDC model are able to precisely predict the main trends of the experiment, such as the modulations of the reaction front position with gravity or the increase of the front width in the shadowgraph under low-g, irrespective of the fact that a quantitative comparison is not possible due to the unknown chemical timescale τ_c. Thus we can use the equations of Sec. 3, together with the knowledge of the computed velocity and concentration fields,[17,18] for an understanding of the phenomena. Applying the curl to eqn (5) we obtain a relationship between the vorticity $\vec{\omega} = \nabla \times \vec{v}$ and the rotational part of the buoyancy term. For the present two-dimensional flow ω has only a y-component, i.e., $\vec{\omega} = \omega \vec{e}_y = (\partial_x v_z - \partial_z v_x)\vec{e}_y$. Thus we arrive at

$$\Delta\omega = \partial_x(R_a a + R_b b + R_s s). \tag{11}$$

Inspecting the x-dependency of the species concentrations in Fig. 13 we note that $|\partial_x a| > |\partial_x b| > |\partial_x s|$. Together with the corresponding Rayleigh number ratios (Sec. 3) we can safely estimate that

$$\omega/L_z^2 \approx R_a\partial_x a < 0 \quad \text{for } x < X_f \tag{12}$$

$$\omega/L_z^2 \approx R_b\partial_x b > 0 \quad \text{for } x > X_f \tag{13}$$

where $\Delta\omega \approx \omega/L_z^2$ was used. Thus we see that the sign of the gradient of $\partial_x c_i$, which arises from the species consumption due to the chemical reaction, defines the sign of the vorticity vector. On the acidic side the vorticity is negative, hence the vortex rotates there counter-clockwise while on the basic side, $\omega > 0$ with a clockwise motion of the vortex. An order-of-magnitude estimate of the amplitude of the velocity, advecting fresh species towards the front, can be gained from $\omega = \partial_x v_z - \partial_z v_x \sim 2v_x/L_z$. Thus the horizontal velocity on the acidic side scales like $v_x \sim L_z^3 R_a \partial_x a/2$, and correspondingly that of the basic side as $v_x \sim L_z^3 R_b \partial_x b/2$. If we now go back to the x-component of the Stokes-eqn (5), $\partial_x p = (\partial_x^2 + \partial_z^2)v_x$, we realise that the horizontal pressure gradient will be different on both sides of the reaction front. Since $\partial_x p$ is higher on the acidic side, the reaction front moves towards the base as observed in both experiments and simulations. Because $\partial_x p$ further scales with the Rayleigh number, hence with the level of gravitational acceleration, an acceleration of the front propagation has to occur under hyper-g leading to the characteristic modulations of the front position in Fig. 5 and 14.

By mimicking the imaging process of the shadowgraph technique used in the experiment, the simulations are also able to link the contrast changes detected in the shadowgraph with the concentration distribution. In this way, the bright trailing edge in the shadowgraphs can be associated with the location of maximum salt concentration which appears at the place of maximum production $\langle ab \rangle$, i.e., at the reaction front position X_f. This reveals the mechanism underlying the increase of the width of the front together with a decrease in the contrast in the shadowgraph. With the transition from the hyper-g towards the low-g phase, the vortex system associated with the front decays on a timescale $\tau_{viscous} \approx v_z^2/\nu \approx 1$ s in the experiment, or remains on a very low level in the numerics since a residual $g = 0.1g_0$ was set there. As a result, the advection of the salt by the flow is terminated. This non-advected amount of salt in low-g gives rise to a modification of the curvature of the concentration profiles, leading to an increase of the width of the front in its shadowgraph representation, see Fig. 13d. In parallel, the front undergoes a fading out since its shadowgraph contrast is dramatically reduced in both experiments (Fig. 6d) and simulations (compare the amplitudes in Fig. 13a and c). This gives an answer to the question on whether the reaction front will disappear during a hypothetically very long zero-g phase. The answer is no, the phenomenon of a propagating RD front remains of course in zero-g[17,18] which can also be concluded from Fig. 13 showing $a = 0 = b$ in a very localised zone under low-g, too. But the shadowgraph technique, although being a versatile tool for visualising many kinds of optical inhomogeneities in fluids, approaches its limits. In the absence of the sharpening effect exerted by the convection onto the concentration profiles, the curvature of the concentration profiles and thus the contrast becomes too low when only reaction and diffusion alone operate in the present system.

5 Conclusions

By measuring the periodic changes from an accelerated front propagation under hyper-gravity towards a slowed down propagation under low gravity we have shown that gravity markedly influences the motion of reaction fronts even in thin fluid layers. This behaviour is caused by the amplification or decay of a buoyancy-driven double vortex surrounding the front when increasing or decreasing the g-level. This double vortex is attached to the reaction front position and advects fresh species towards the front. The numerical simulations of the experimental shadowgraph visualization have been proved to be a valuable tool especially when more than two species are present. In this way the observations in the shadowgraph of an increasing front width at decreased contrast during low-g could be deciphered as related to a change in the curvature of the concentration profiles. We hope that this approach will stimulate further studies in this direction.

References

1 I. Nagypal, G. Bazsa and I. R. Epstein, *J. Am. Chem. Soc.*, 1986, **108**, 3635–3640.
2 M. Böckmann and S. C. Müller, *Phys. Rev. Lett.*, 2000, **85**, 2506–2509.
3 D. Horváth, T. Bánsági and A. Tóth, *J. Chem. Phys.*, 2002, **117**, 4399–4402.
4 J. D'Hernoncourt, A. Zebib and A. De Wit, *Chaos*, 2007, **17**, 013109.
5 L. Rongy, G. Schuszter, Z. Sinkó, T. Tóth, D. Horváth, A. Tóth and A. De Wit, *Chaos*, 2009, **19**, 023110.
6 M. Wiedemann, V. M. Fernandes de Lima and W. Hanke, *Phys. Chem. Chem. Phys.*, 2002, **4**, 1370–1373.
7 H. Miike, H. Yamamoto, S. Kai and S. C. Müller, *Phys. Rev. E*, 1993, **48**, R1627–R1630.
8 L. Gálfi and Z. Rácz, *Phys. Rev. A*, 1988, **38**, 3151–3154.
9 Z. Jiang and C. Ebner, *Phys. Rev. A*, 1990, **42**, 7483–7486.
10 A. Zalts, C. El Hasi, D. Rubio, A. Ureña and A. D'Onofrio, *Phys. Rev. E*, 2008, **77**, 015304.
11 C. Almarcha, P. M. J. Trevelyan, P. Grosfils and A. De Wit, *Phys. Rev. Lett.*, 2010, **104**, 044501.
12 C. Almarcha, Y. R'Honi, Y. De Decker, P. M. J. Trevelyan, K. Eckert and A. De Wit, *J. Phys. Chem. B*, 2011, **115**, 9739–9744.
13 S. Kuster, L. A. Riolfo, A. Zalts, C. El Hasi, C. Almarcha, P. M. J. Trevelyan, A. De Wit and A. D'Onofrio, *Phys. Chem. Chem. Phys.*, 2011, **13**, 17295–17303.
14 K. Eckert and A. Grahn, *Phys. Rev. Lett.*, 1999, **82**, 4436–4439.
15 K. Eckert, M. Acker and Y. Shi, *Phys. Fluids*, 2004, **16**, 385–399.
16 Y. Shi and K. Eckert, *Chem. Eng. Sci.*, 2006, **61**, 5523–5533.
17 L. Rongy, P. M. J. Trevelyan and A. De Wit, *Phys. Rev. Lett.*, 2008, **101**, 084503.
18 L. Rongy, P. M. J. Trevelyan and A. De Wit, *Chem. Eng. Sci.*, 2010, **65**, 2382–2391.
19 S. Fujieda, Y. Mogamia, A. Furuya, W. Zhang and T. Araiso, *J. Phys. Chem. A*, 1997, **101**, 7926–7928.
20 S. Fujieda, Y. Mori, A. Nakazawa and Y. Mogami, *Adv. Space Res.*, 2001, **28**, 537–543.
21 Y. Shi, K. Eckert, A. Heinze and M. Acker, *17th ESA Symposium on European Rocket and Balloon Programmes and Related Research*, 30 May–2 June 2005, Sandefjord, Norway, 2005, pp. 545–550.
22 D. Bratsun and A. De Wit, *Chem. Eng. Sci.*, 2011, **66**, 5723–5734.
23 Y. Shi and K. Eckert, *Chem. Eng. Sci.*, 2008, **63**, 3560–3563.
24 A. Heinze, K. Eckert, M. Hauser and S. Odenbach, *Acta Astronaut.*, 2011, **68**, 707–716.
25 W. Merzkirch, *Flow Visualization*, Academic Press Inc., 1987.
26 L. Rongy and A. De Wit, *J. Chem. Phys.*, 2006, **124**, 164705.